Received: 19 August 2020 | Revised: 15 April 2021 | Accepted: 16 April 2021

DOI: 10.1002/eqe.3469

WILEY

RESEARCH ARTICLE

Experimental seismic performance assessment and numerical modelling of nonlinear inerter vibration absorber (IVA)-equipped base isolated structures tested on shaking table

Daniele Pietrosanti[1] | **Maurizio De Angelis**[1] | **Agathoklis Giaralis**[2]

[1] Department of Structural and Geotechnical Engineering, Sapienza University of Rome, Rome, Italy

[2] Department of Civil Engineering, City University of London, London, United Kingdom

Correspondence
Maurizio De Angelis, Department of Structural and Geotechnical Engineering, Sapienza University of Rome, Via Eudossiana 18, 00184 Rome, Italy.
Email: maurizio.deangelis@uniroma1.it

Funding information
Sapienza University of Rome, Grant/Award Number: RP1181643697C751

Abstract

In recent years, inerter vibration absorbers (IVAs), such as the tuned mass damper inerter (TMDI), attracted much attention in the literature for reducing seismic displacement demands of base isolated structures (BISs). Several theoretical studies reported reduced BIS seismic demands with increasing inertance endowed by a grounded inerter element, but adopted mostly idealized linear dynamical models. Herein, the potential of TMDI-configured IVAs for seismic response reduction of BISs modelled as single-mass structures is assessed under the combined effects of nonlinear inerter and structural behavior. To this aim, experimental data from a shaking table testing campaign are considered utilizing a custom-built flywheel rack-and-pinion grounded inerter prototype with variable inertance, along with high damping rubber bearings in the isolation layer and in the BIS-to-absorber link. White noise excitation and an ensemble of six ground motions (GMs) with different frequency content are used in the tests for which bearings exhibit softening nonlinear behavior. Experimental results demonstrate improvement of BIS nonlinear seismic response in terms of displacement and base shear with increasing inertance for nonlinear and nonoptimally tuned IVAs. It is found though that the considered IVAs may be detrimental to BIS acceleration response depending on the GMs time-varying frequency content signatures as captured by the continuous wavelet transform spectrogram. Finally, it is concluded that representing the inerter device by a simplified linear dissipative model as opposed to a nonlinear model with friction and gear backlash suffices to trace the BIS response with acceptable accuracy and, thus, can be used for optimal seismic TMDI design.

KEYWORDS
base isolated system (BIS), experimental parametric analysis, inerter, nonlinear models, seismic effectiveness, tuned mass damper inerter (TMDI)

1 | INTRODUCTION

Over the past three decades, the concept of base isolation has proved its worth in achieving high seismically performing structures, including bridges[1] and buildings,[2,3] as well as in protecting critical structures, including hospitals,[4,5] nuclear power plants,[6,7] offshore structures,[8] and sensitive secondary components[9–11] from earthquakes. Base isolation is implemented through laterally flexible bearings placed in between the structure/object and its foundation/base which elongate significantly the fundamental structural natural period. Under typical horizontal seismic ground motion excitations (GMs), this provision reduces appreciably the lateral seismic forces imparted to the base isolated structure (BIS). It further reduces deformations to the isolated superstructure (eg, storey drifts in buildings), which tend to perform lateral rigid body-like translations, thus, mitigating structural damage risk. However, the above benefits come at the price of considerable lateral deformation demands posed to the bearings which, in conjunction with record-to-record uncertainty/variability, may increase the collapse probability of BISs to unacceptable levels unless sufficient lateral deformation bearing capacity is provided.[12] The latter provision increases the cost of bearings and of the BIS, as requirements for flexible utility ducts and services as well as for sufficient clearance around structures to minimize risk of collisions.

Recognizing that supplemental damping can effectively reduce seismic demands in BISs,[5,13] several researchers investigated the use of passive dynamic vibration absorbers for the task. Specifically, Yang et al.[14] and Tsai[15] showed numerically that conventional tuned mass dampers (TMDs) comprising an oscillating secondary mass attached to the isolation layer via a viscoelastic link (ie, linear spring/stiffener in parallel with a linear viscous damper) can reduce seismic drift demands in base isolated multistorey buildings. Further, Taniguchi et al.[16] considered the response of TMD-equipped BISs modelled as linear single degree of freedom (SDOF) systems exposed to several recorded GMs and showed that TMDs can reduce peak BIS displacement and, for some of the GMs, peak BIS acceleration as well. Additionally, Petti et al.[17] confirmed experimentally the above TMD benefits through shaking table testing of a scaled-down TMD-equipped BIS subject to recorded GMs. More recently, De Domenico and Ricciardi[18] presented a numerical case study of a real-life base isolated building structure with a TMD at its basement and demonstrated improved seismic response under artificial design spectrum compatible GMs. Still, previous studies found that excessively large oscillating TMD mass (ie, 18% the BIS mass or more) is required to achieve substantial BIS displacement demand reductions[15,18] while peak TMD mass displacement can be up to four times larger than the peak bearings displacement.[16]

To this end, recent numerical studies[19–23] showed that the above shortcomings of the TMD for seismic motion control of BISs can be rectified by leveraging the inertial amplification effect of a grounded *ideal inerter*,[24] also referred to as gyro-mass damper.[25] Note that the ideal inerter is a linear massless mechanical element resisting relative acceleration by a proportionality constant termed *inertance* and measured in mass (kg) unit.[24] Therefore, supporting the TMD secondary mass to the ground through an inerter yields a linear inerter-based vibration absorber (IVA) configuration, termed tuned mass-damper-inerter (TMDI) in the literature,[26–28] with total inertia given by the sum of the inertance and the secondary mass. In this regard, it is found that the TMDI with grounded inerter requires significantly less secondary mass to achieve the same seismic control performance for BISs as the TMD assuming linear[20,23] and nonlinear[21] isolation bearings. At the same time, the inclusion of the grounded inerter reduces significantly the secondary mass displacement.

Importantly, the assumption of a massless inerter with very large inertance (ie, one order of magnitude lower than the BIS mass) made in all the above numerical studies on TMDI-equipped BISs is largely realistic since physical inerter devices with inertance scaling-up independently of the physical device mass have been prototyped and experimentally verified. Devices include mechanical inerters using rack-and-pinion[29,30] and ball-screw mechanisms[31,32] to transform translational motion into rotational motion of a flywheel (ie, a lightweight fast spinning disk), hydraulic inerters using hydraulic motors for the same task,[33,34] and fluid inerters relying on the inertia of liquid forced into a helical tube with small cross-section.[35,36] Full-scale inerter devices developed for earthquake applications include the mechanical ball-screw inerter in Nakamura et al.[32] achieving inertance of 8000 tons and the hydraulic inerter in Nakaminami et al.[34] reaching inertance of more than 10 000 tons. Nevertheless, experimental dynamic testing of inerter devices demonstrate deviation from the ideal inerter element behavior assumed in the previously reviewed theoretical studies due to various effects dependent on the specifications, operational frequency range, and technology used to implement the inerter (ie, mechanical, hydraulic, or fluid). In this respect, assessing the influence of nonideal inerter behavior to inerter-based vibration absorbers becomes important[37]. To this aim, De Domenico et al.[39] conducted pertinent computational work in which parametric force-deformation relationships of nonideal inerters have been incorporated into the equations of motion of TMDI-equipped BISs and solved for a large number of recorded GMs assuming linear structural behavior. These force-deformation relationships have been calibrated against experimental data derived from dynamic testing of a physical fluid

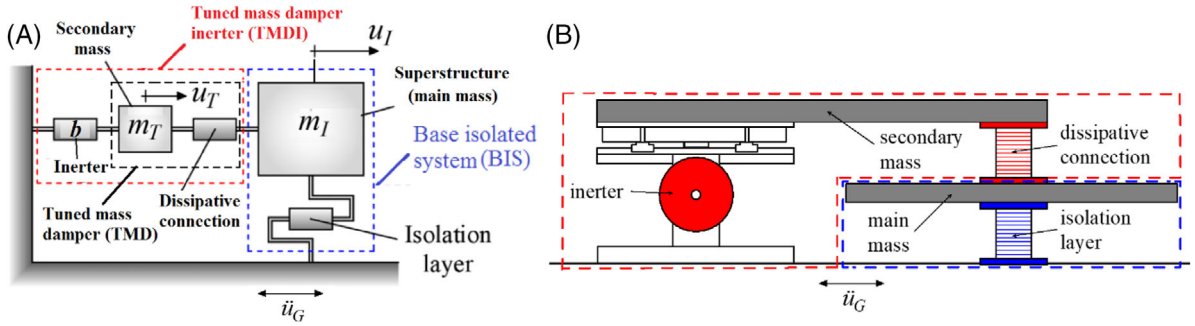

FIGURE 1 Lumped-mass model of SDOF base isolated structure (BIS) with attached tuned mass damper inerter (TMDI), (A) Idealization, (B) Physical model conceptualization

inerter prototype. However, this approach cannot capture potential interaction effects of the nonideal inerter with the TMD and the BIS. To this end, Gonzales-Buelga et al.[40] considered real-time dynamic hybrid testing (substructuring) of an IVA termed tuned inerter damper (TID), that is, a TMDI with no secondary mass introduced by Lazar et al.,[38] attached to a linear structure and featuring a physical commercial grounded inerter. The latter device was small scale, achieving about 80 kg of inertance, while the remainder of the TID and the SDOF oscillator were computer simulated assuming linear behavior. Further, Brzeski et al.[30] built a large-scale IVA, featuring a mechanical (rack and pinion) flywheel inerter with continuously varying transmission to change inertance, and tested it experimentally in a rig with an embedded linear damped structure under harmonic excitation.

In view of the above, to date, all research studies which accounted for nonideal inerter behavior in assessing the potential of various IVAs for earthquake protection of BISs, assumed overall linear structural behavior. However, under strong earthquake excitation, base isolators as well as the IVAs may behave in a nonlinear fashion. To this end, this article aims to evaluate the effectiveness of IVAs with grounded inerter to mitigate the seismic response of BISs as nominal inertance value increases by taking into account the nonlinear behavior of the isolators and of the viscoelastic link of the secondary mass to the BIS as well as the nonideal physical inerter device. This is pursued by considering experimental data from a shaking table testing campaign involving physical specimens of single-mass BISs equipped with nonoptimal IVAs in the TMDI configuration. It is noted in passing that the same specimens have been recently used by the authors to study the response of IVA-equipped structures under harmonic excitations focusing on mechanical engineering applications.[41,42] Herein, nonlinear response experimental data from shaking table testing under white noise and recorded GM excitations are considered with time scaling relevant to large-scale BISs encountered in earthquake engineering applications. Attention is focused on data interpretation in terms of BIS and secondary mass displacements and accelerations as well as in terms of forces developing in the isolators and the inerter against the time-varying frequency content of different near- and far-field GMs as captured by wavelet transform GM analysis. Further, parametric numerical models of varying sophistication are considered to approximate the experimentally measured response of the physical specimens accounting for the nonlinear behavior of the isolators as well as the nonideal inerter device considered in the shaking table testing.

The remainder of the article is organized as follows. In Section 2, the physical models and the shaking table setup, including instrumentation, are described. Section 3 discusses experimental data for white noise excitation used for characterizing the dynamic behavior of the specimens. In Section 4, the response of specimens to various GMs is appraised accounting for different levels of intensity and excitation frequency content. Section 5 presents a parametric numerical model calibrated against experimental data and assesses its potential to characterize the specimens under earthquake excitation, while Section 5 summarizes concluding remarks.

2 | SHAKING TABLE TESTING CAMPAIGN

2.1 | Physical modelling of IVA-equipped base isolated structures

Consider a planar BIS with rigid superstructure represented by a lumped mass, m_I, resting on a flexible isolation layer as depicted in Figure 1A. The oscillating mass of the isolation system is included within m_I and, therefore, a single coordinate, u_I, hereafter defined as the relative displacement of the mass m_I with respect to the ground, suffices to describe the dynamic response of the BIS under horizontal support acceleration $\ddot{u}_G$. This simplified SDOF modelling of the BIS is relevant to different types of BISs including stiff low-rise base isolated buildings,[16] decks of isolated bridges along their

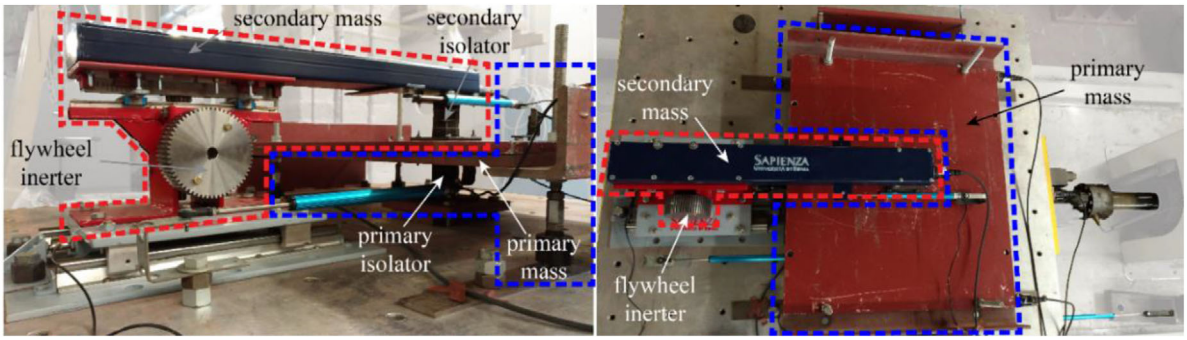

FIGURE 2 Physical specimen mounted on shaking table

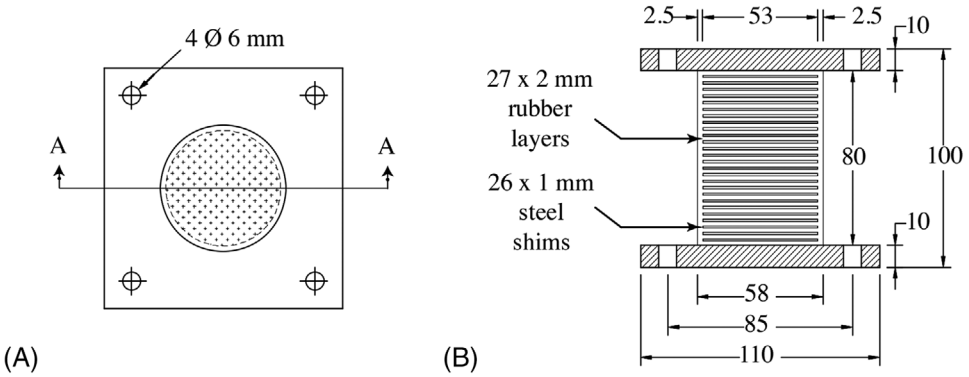

FIGURE 3 High damping rubber bearing (HDRB) isolators: (A) Plan view and (B) section A-A

longitudinal direction,[43] base isolated storage tanks,[9,44] and block-type secondary equipment and artefacts anchored on floor isolation systems within buildings.[10,11] A passive TMD with secondary mass m_T is attached to the BIS as shown in Figure 1A via a dissipative connection, commonly taken as linear viscoelastic element,[16] to suppress the lateral deformation of the isolation layer. Further, the TMD is supported to the ground by an inerter element with inertance, b, resulting in the TMDI vibration absorber. The latter was introduced by Marian and Giaralis[26] and subsequently considered in several numerical studies[20–23,28,39,45] for seismic protection of BISs.

Herein, the response of the 2-DOF hybrid vibration control system in Figure 1A to earthquake excitation is studied experimentally via shaking table testing. In the experimental campaign, the effects of both the secondary mass and the inertance are parametrically investigated. This is because the secondary mass governs the motion control potential and the monetary cost of dynamic vibration absorbers, while previous theoretical work[23] demonstrate that the inertance can substitute secondary mass for fixed BIS performance leading, ultimately, to more lightweight absorbers. Theoretically, this can be readily understood by noting that the grounded inerter acts as a mass with inertia b, which can be orders of magnitude higher from the physical device mass.[24] It, therefore, increases the inertia of the secondary mass from m_T to $m_T + b$ with insignificant weight increase. To this end, a series of physical specimens, conceptualized in Figure 1B, with different inertance and secondary mass are built on a shaking table. All specimens have the same main mass, $m_I = 125kg$, consisting of two steel plates bolted together as seen in Figure 2 which includes side and aerial view photos of a sample specimen. Further, in all the specimens, the same cylindrical high damping rubber bearing (HDRB) is used in the isolation layer (primary isolator) and in the dissipative connection (secondary isolator) shown in Figure 3. Total rubber thickness is 54 mm and the height of the isolator excluding the end plates is 80 mm.

Inertance is provided to the specimens by a custom-built device employing a rack-and-pinion mechanism to transform relative translational motion between the secondary mass and the shaking table to rotational motion of a flywheel. A picture of the standalone inerter device is shown in Figure 4 together with an exploded three-dimensional drawing of all device components made of steel. The device chassis is in-house machined. It supports an off-the-shelf gearbox with fixed gear ratio 2:1 used to amplify the flywheel angular velocity. The rack has square section 20 × 20 mm with length 300 mm and is mounted on a slide with ±55 mm of maximum stroke. Its translational motion causes rotation to the spur gear pinion with diameter 36 mm and tooth width 25 mm. The latter is mounted on the gearbox input shaft. The nominal inertance of

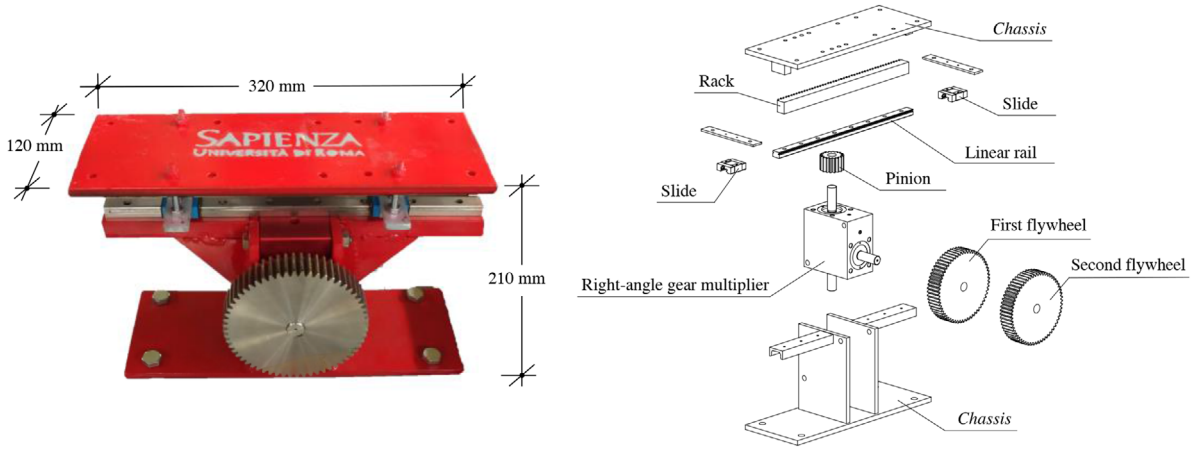

FIGURE 4 Custom-built rack-and-pinion flywheel-based inerter prototype used in the physical models

TABLE 1 Inertial properties of the TMDI-configured physical IVAs and inertance/mass ratios $\delta = \beta/\mu$

	Secondary mass ratios		
Inertance ratios	**Small mass (SM) ($\mu_1 = 0.048$)**	**Medium mass (MM) ($\mu_2 = 0.080$)**	**Large mass (LM) ($\mu_3 = 0.160$)**
No flywheel (NF) ($\beta_1 = 0.001$)	0.021	0.013	0.006
Medium flywheel (MF) ($\beta_2 = 0.383$)	7.800	4.789	2.394
Large flywheel (LF) ($\beta_3 = 0.765$)	15.938	9.563	4.781

the device depends on the flywheel mass moment of inertia attached to the output gearbox shaft. Herein, three different inertance values, b, are considered: no flywheel (NF case) with very low nominal inertance $b_1 = 0.1kg$; medium flywheel (MF case) with nominal inertance $b_2 = 47.9kg$ where one spur gear with diameter 120 mm and mass 2.1 kg is attached to the gearbox; large flywheel (LF case) with nominal inertance $b_3 = 95.6kg$, where two same spur gears are attached to the gearbox. The corresponding inertance ratios, $\beta = b/m_I$ of the specimens are reported in Table 1. Meanwhile, the physical mass of the inerter contributing to the relative kinematics of the specimens with respect to the shaking table is approximately 2 kg pertaining only to the rack of the device and to the connecting end plate above the rack (Figure 4). Importantly, this "suspended" mass is independent of the flywheel mass since, purposely, the flywheel is mounted to the lower part of the inerter device which is practically nondeformable and rigidly fixed to the shaking table. In this regard, this tailor-made device meets the criteria of an inerter[46] as its contributing mass to deflections relative to the ground dynamics is independent of the nominal inertance which can scale up either by using larger flywheels, as detailed above, or by increasing the gearbox ratio.

Furthermore, specimens with three different secondary masses, m_T have been tested with mass ratios $\mu = m_T/m_I$, reported in Table 1 which include the suspended inerter mass of 2.0 kg. The small mass (SM) specimens with $m_T = 6kg$ yields a mass ratio of about 5% herein treated as a low bound value for inertial absorbers in earthquake engineering applications.[47] The large mass (LM) specimens with $m_T = 20\,kg$ and mass ratio of 16% are taken as paradigms of heavyweight inertial absorbers while the medium mass (MM) specimens with $m_T = 10\,kg$ and mass ratio of 8% refer to intermediate weight absorbers (Figure 2 shows a MM specimen with LF). Understandably, the different TMDI-configured IVAs studied in the experimental campaign are not optimally tuned to any structural response criterion. In this setting, detuning effects due to nonlinear response of specimens do not overshadow the main aim of this study which is to quantify the relative effect of increasing the inertance vis-à-vis increasing the secondary mass to the response of BISs under seismic excitation of increasing intensity accounting for nonlinear structural behavior and nonideal inerter behavior.

2.2 | Shaking table specifications and instrumentation

Testing was carried out on the $1.50m \times 1.50m$ uniaxial shaking table facility in the Department of Structural and Geotechnical Engineering at Sapienza, University of Rome. All specimens were instrumented as detailed in Figure 5 by:

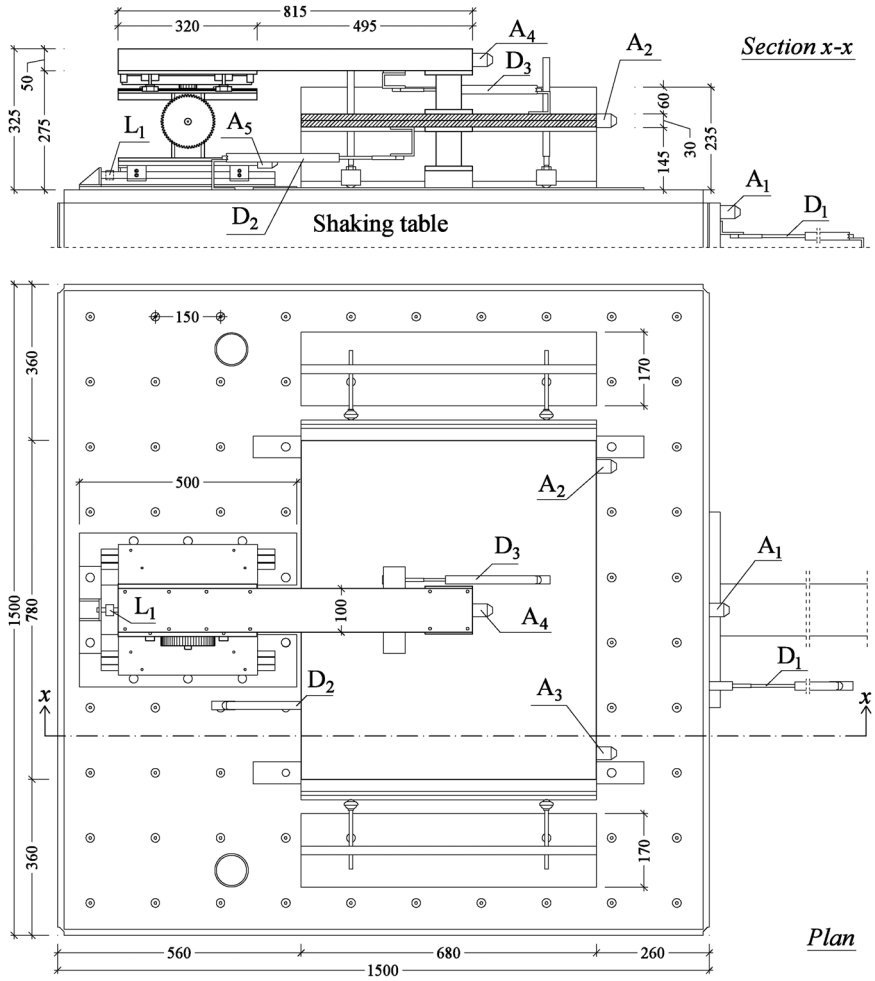

FIGURE 5 Schematic of the experimental setup and instrumentation

Sensor	A_1	A_2	A_3	A_4	A_5	D_1	D_2	D_3	L_1
Quantity	$\ddot{u}_G$	$\ddot{u}_{I,r}^{(tot)}$	$\ddot{u}_{I,l}^{(tot)}$	$\ddot{u}_T^{(tot)}$	$\ddot{u}_B^{(tot)}$	u_G	u_I	u_{TI}	F_R

- Five piezoelectric accelerometers. One placed on the shaking table measuring input horizontal ground acceleration, $\ddot{u}_G$; two placed on the main mass measuring total horizontal response acceleration, $\ddot{u}_{I,r}^{(tot)}$ and $\ddot{u}_{I,l}^{(tot)}$, at two different locations as indicated in Figure 5; one placed on the secondary mass measuring total horizontal response acceleration $\ddot{u}_T^{(tot)}$; and one at the inerter support measuring $\ddot{u}_B^{(tot)}$.
- Three displacement sensors measuring relative displacement between (i) the shaking table mass and the lab floor (fixed reference point), u_G, (ii) the primary mass and the shaking table mass, u_I, and (iii) the secondary mass and the primary mass, $u_{TI} = u_T - u_I$
- A load cell measuring the force transmitted by the grounded terminal of the inerter to the shaking table F_R.

Experimental data series were acquired at 500 Hz and band pass filtered by a first-order Butterworth filter within the frequency range (0.16-20 Hz). Based on the above measured quantities, the following responses of interest are computed as follows:

- absolute $\ddot{u}_I^{(tot)} = (\ddot{u}_{I,l}^{(tot)} + \ddot{u}_{I,r}^{(tot)})/2$
- relative $\ddot{u}_T = \ddot{u}_T^{(tot)} - \ddot{u}_B^{(tot)}$, where the acceleration $\ddot{u}_B^{(tot)}$ differs insignificantly with respect to $\ddot{u}_G$ as verified during testing;
- relative $u_T = u_I + u_{TI}$;

TABLE 2 Recorded acceleration ground motions considered in the seismic effectiveness evaluation

Event	Magnitude	GM record station	PGA (g)	Duration (s)	Epicentral distance (km)	Attributes
Irpinia, Italy (1980)	6.9	Sturno	0.232	39.3	30.4	Fault-normal with pulse of period 3.1 s[48]
Cape Mendocino, CA (1992)	7.0	Petrolia	0.615	36.0	4.5	Near-fault with pulse of period 3.0 s[48]
Northridge, CA (1994)	6.7	Sylmar–Olive View	0.568	39.9	16.8	Near-fault with pulse of period 3.1 s[48]
Kobe, Japan (1995)	6.9	KJMA	0.345	40.4	1.0	Near-fault with pulse of period 1 s[23]
Imperial Valley, CA (1940)	7.0	El Centro Array # 9	0.315	39.5	6.1	Near-fault pulse-free rich in high frequencies[23]
Tokachi-Oki, Japan (1968)	7.9	Hachinohe	0.229	43.5	>100	Far-field broadband[49]

- resisting force generated by the inerter device as in $F_B = F_R + m_B \ddot{u}_B^{(tot)}$, where m_B is the nonsuspended inerter mass corresponding to the nondeformable part of the inerter below the rack (see also Ref. [46]) which is equal to 16.7, 18.8, and 20.9 kg for the NF, IF, and LF specimens, respectively;
- resisting $F_T = -F_B - m_T \ddot{u}_T^{(tot)}$;
- and resisting force generated at the primary isolator as in $F_I = F_T - m_I \ddot{u}_I^{(tot)}$.

2.3 | Dynamic excitations

Seismic tests to all the 9 IVA-equipped BIS specimens listed in Table 1 as well as to the uncontrolled BIS (no IVA attached) have been conducted for two different types of dynamic excitations at various amplitudes. First, white noise acceleration excitation band-limited within [0.5 10] (Hz) interval with three different amplitudes A_j; $j = 1 - 3$ corresponding to variance, $\sigma^2_{\ddot{u}_G}$, equal to 0.099, 0.916, and 2.605 m^2/s^4 were considered. The duration of the excitation signals was 60 s long which was sufficient for all specimens to reach steady-state response conditions. Further, all specimens were tested for the 6 recorded GMs listed in Table 2, spanning a wide range of peak ground accelerations (PGA) and frequency domain properties. The GM signals were applied unscaled as well as scaled by a factor of two to gauge the influence of nonlinear effects to the response of the specimens.

Importantly, the design shear strain of the HDRB isolators is not exceeded under any of the dynamic excitations herein considered. Moreover, the time scale of all the excitation signals is compressed by a scaling factor of 0.2. The basis of selecting this scaling factor is to ensure that the scaled-down physical models used in the experimental campaign are representative of full-scale BISs. In particular, the effective natural period of the uncontrolled physical model for shear deformation 100% of the primary isolator is 2.65 s in the unscaled time axis (0.52 s in the scaled time axis) which is a reasonable specification of real-life BIS designs.

3 | DYNAMIC RESPONSE CHARACTERIZATION UNDER WHITE NOISE EXCITATION

This section furnishes and discusses selective experimentally derived frequency response functions (FRFs) as well as force-deformation curves obtained from different physical specimens detailed in the previous section under white noise excitation. Effective natural frequencies and critical damping ratios derived from the experimental data are also provided. The aim is to gain insights to the dynamic response of the IVA-equipped BIS specimens as inertance as well as excitation amplitude and, thus, level of nonlinear behavior, vary. In this regard, normalized FRFs for various response quantities defined as:

$$\widehat{H}_d = H_d / H_{(\ddot{u}_G)}; d = u_I, \ddot{u}_I^{(tot)}, F_I, u_{TI}, \ddot{u}_I^{(tot)}, F_T, u_T, \ddot{u}_T, F_B, \tag{1}$$

are considered. In the last equation, H_d is the FRF of the dth response quantity and $H_{\ddot{u}_G}$ is the FRF of the white noise excitation signals.

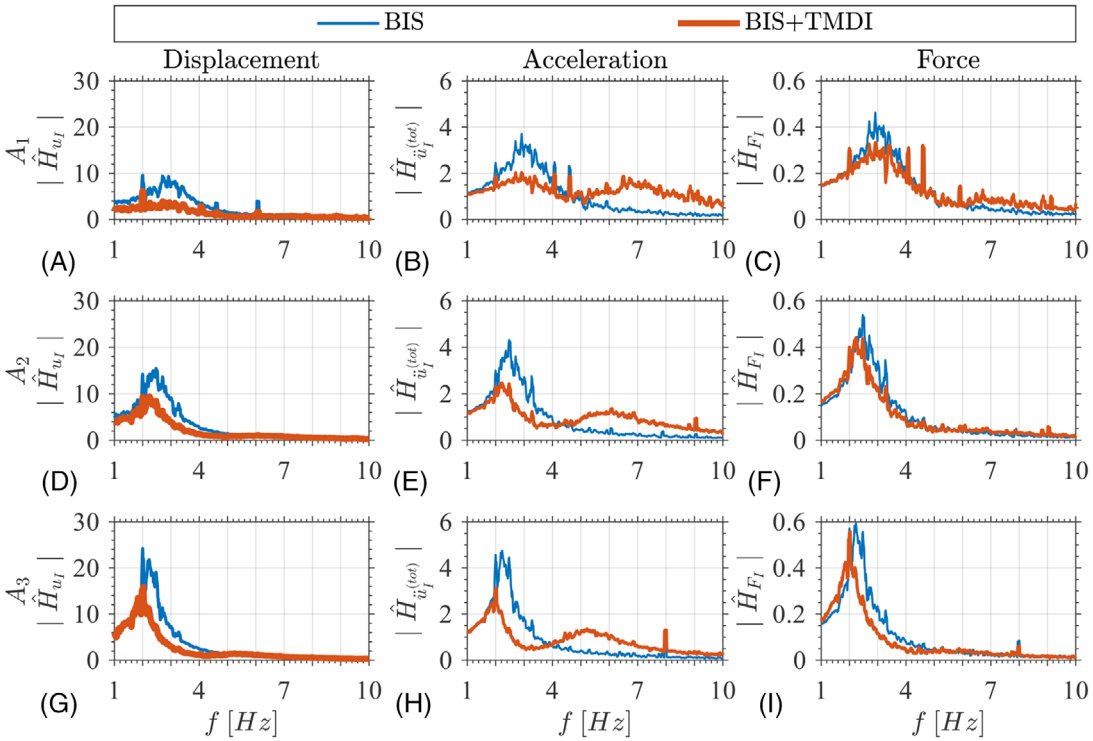

FIGURE 6 Normalized FRFs of BIS displacement, BIS acceleration, and primary isolator shear force, under random white noise excitation at three different amplitudes for uncontrolled BIS and for the IVA-controlled BIS (BIS + TMDI) with $\beta_2 = 0.383$ and $\mu_2 = 0.080$

Figure 6 plots normalized FRFs of the displacement, acceleration, and base shear of the primary isolator of the uncontrolled BIS specimen and of the BIS controlled by the medium mass and MF IVA subjected to three white noise excitation signals with different amplitudes specified in Section 2.3. It is seen that the (single) resonant frequency of the uncontrolled BIS reduces as the excitation amplitude increases indicating stronger nonlinear behavior of the softening kind. Further, the inclusion of the IVA adds a second (higher) resonant frequency to the BIS which is mostly visible in the BIS acceleration FRF since response acceleration signals are influenced more by high-frequency system dynamics. This second resonant frequency corresponds to an out-of-phase motion between primary and secondary mass.[18,42] Importantly, the considered TMDI-configured IVA suppresses appreciably the coordinates of all the FRFs of the uncontrolled BIS for frequencies below 4 Hz associated with the (first) BIS resonant frequency. However, the IVA significantly amplifies acceleration FRF coordinates of the BIS for frequencies higher than 4 Hz. Similar trends have been observed to the FRFs of the rest of the specimens, not included here for brevity. In this regard, the considered nonoptimal TMDI-configured IVA is expected to always reduce BIS displacement demands but not necessarily BIS acceleration demands, the latter being heavily dependent on the excitation frequency content.

Evidence of the nonlinear response of the primary isolator is provided in Figure 7 plotting force-deformation curves of the primary isolator, $F_I - u_I$, for the specimens considered in Figure 6 under white noise excitations with different amplitudes. Clear hysteretic loops form for both the uncontrolled and the controlled BIS. The area of these loops, and thus, the energy dissipated by the primary isolator, increases with increasing excitation amplitude. Additionally, the slope of the backbone curve also increases with excitation amplitude manifesting softening nonlinear behavior which is also related to the shift of the (first) BIS resonant frequency to the left in the FRFs of Figure 6. To further quantify the softening of the primary isolator of the physical specimens under increasing excitation amplitude, Table 3 reports the effective natural frequencies, periods, and critical damping ratio properties derived from experimental steady-state dynamic response data presented in Figure 7 to white noise excitations at three different amplitudes. These properties have been obtained by considering equivalent viscoelastic systems using the approach detailed in Luş et al.[50] It is found that the effective period of the primary isolator is elongated with the excitation amplitude. More importantly, it is seen that the identified effective properties of the physical specimens in the unscaled time axis are representative of common real-life base isolated structures with HDRBs both in terms of effective natural periods, which range within 1.5 to 2.5 s and of critical damping ratios, which range within 16 to 24.6%.

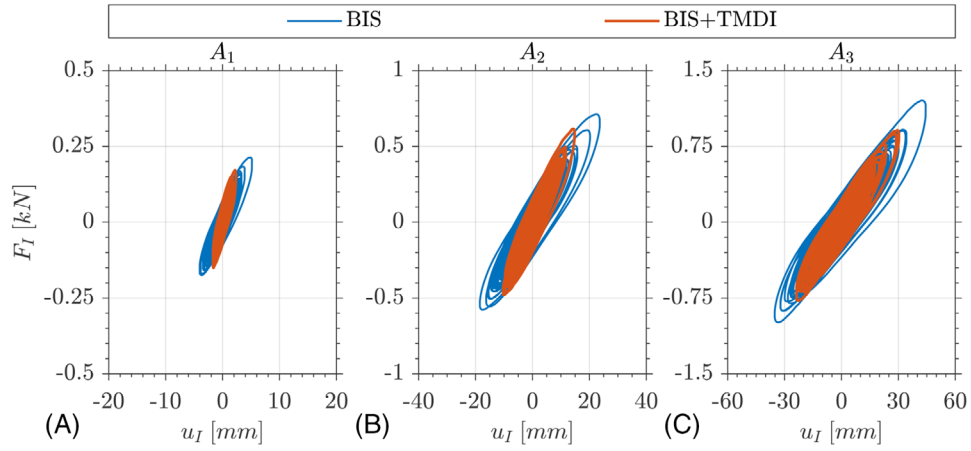

FIGURE 7 Force-deformation curves, $F_I - u_I$, of uncontrolled BIS and for BIS with TMDI-configured IVAs with $\beta_2 = 0.383$ and $\mu_2 = 0.080$ under random white noise excitation at three different amplitudes

TABLE 3 Effective natural frequency, f, natural period, T, and critical damping ratio ξ of the primary and secondary isolators derived from the experimental data of Figure 7

White noise amplitude		***A*₁**		***A*₂**		***A*₃**	
	f (Hz)	3.26		2.69		2.45	
	T (s)	0.31 (1.54)*		0.37 (1.86)*		0.41 (2.04)*	
	ξ (%)	19.12		17.90		15.87	
BIS + TMDI	Isolator	I	II	I	II	I	II
	f (Hz)	3.34	7.09	2.37	6.32	2.01	5.53
	T (s)	0.30 (1.50)*	0.15 (0.71)*	0.42 (2.11)*	0.16 (0.79)*	0.50 (2.49)*	0.18 (0.90)*
	ξ (%)	24.58	20.00	21.24	18.21	18.21	15.81

*Effective period in the "real" scale (time scale reduction factor 0.2).

Interestingly, Figure 7 suggests that the energy dissipated by the primary isolator reduces somewhat with the inclusion of the absorber. Nevertheless, the force-deformation curves of the secondary isolator, $F_T - u_{TI}$, in Figure 8A for the previously considered IVA-equipped BIS exposed to different amplitude white noise excitation demonstrate that the dissipated energy at the TMDI (secondary) isolator increases significantly with excitation amplitude. They further demonstrate nonlinear softening behavior of the isolator with increase displacement following the increase

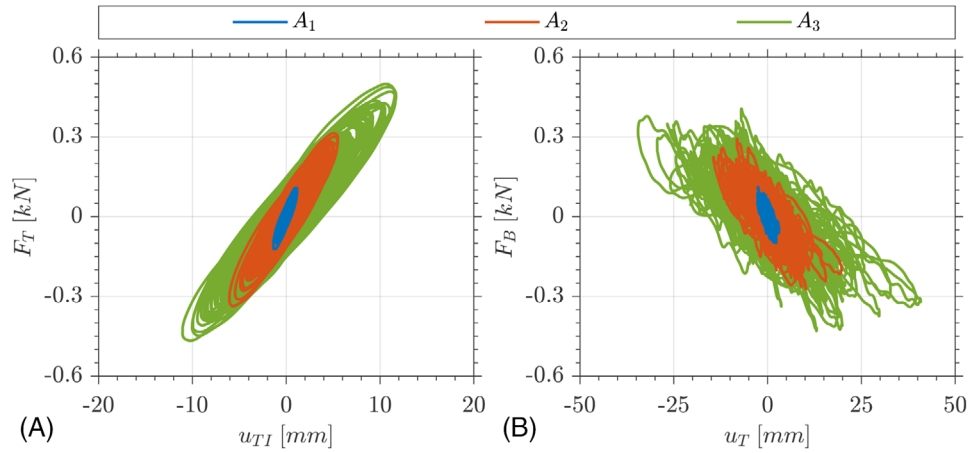

FIGURE 8 Force-deformation curves (A) $F_T - u_{TI}$ and (B) $F_B - u_T$ of BIS equipped with TMDI-configured IVAs with $\beta_2 = 0.383$ and $\mu_2 = 0.080$ under random white noise excitation at three different amplitudes

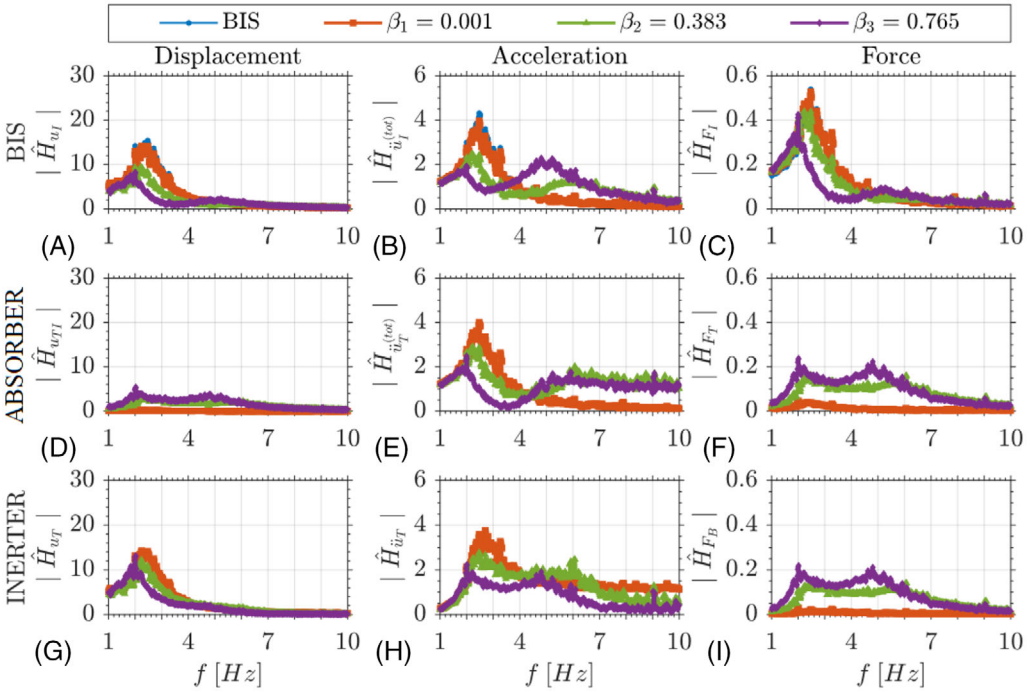

FIGURE 9 Normalized FRFs of (A) BIS mass displacement, (B) BIS mass acceleration, (C) BIS isolator shearing force, (D) IVA stroke, (E) secondary mass acceleration, (F) secondary isolator shearing force, (G) secondary mass displacement, (H) inerter relative acceleration, and (I) inerter force of BIS equipped with TMDI-configured IVAs with mass ratio $\mu = 0.080$ and various inertance ratios under random white noise excitation with A_2

excitation amplitude. Moreover, energy is also dissipated at the inerter device as seen in the force-deformation curves, $F_B - u_T$, plotted in Figure 8B for the same specimens. Collectively, the energy dissipated at the secondary isolator and at the inerter explains the BIS response mitigation achieved by the absorber as seen in the FRFs of Figure 6. At the same time, the dissipative behavior of the inerter device considered in the experiments manifest a deviation from the ideal inerter element which is nondissipative by its definition.[24] Still, the average backbone of the inerter force-deformation curves in Figure 8B has a negative slope confirming the interpretation of the inerter as a negative stiffness device[51] naturally occurring by its positive force-acceleration relationship.

To examine the influence of the inertance to the TMDI-configured IVA motion control potential, Figures 9 and 10 furnish experimental FRFs and force-deformation curves, respectively, for IVA-equipped BISs with the same secondary mass but different inertance under the same amplitude white noise excitation. Specifically, Figure 9 plots FRFs of displacement, acceleration, and force quantities (column-wise panel arrangement in the figure) relevant to the primary isolator (ie, isolation layer of the BIS), the secondary isolator (ie, absorber viscoelastic link), and the inerter device (row-wise panel arrangement in the figure). It is seen that both resonant frequencies (ie, location of local FRF peaks) of the IVA-equipped specimens decrease with increasing inertance, with the higher resonant frequency being mostly evident in the acceleration and absorber FRFs. Further, FRF displacement and acceleration amplitudes close to the first resonant frequency reduce with increasing inertance and the same is seen for the shearing force developing at the primary isolator. Note, however, that BIS absolute acceleration amplitude at secondary excitation frequency increases with increasing inertance which demonstrates that increase of inertance may not necessarily be beneficial across all excitation frequencies and response quantities. Last, the FRFs of the absorber control force exerted to the main mass as well as of the inerter force are rather flat/broadband and increase significantly going from negligible inertance (NF) to intermediate inertance (MF), but not quite as much going from MF to large inertance (LF). Thus, developing forces within the IVA increase with inertance but at a reduced rate.

The influence of the inertance to the balance of energy dissipation between primary isolator (isolation layer of the BIS) and secondary isolator (vibration absorber) is demonstrated by the force-deformation curves in Figure 10A and B. It is seen that energy dissipation at the primary isolator is significantly reduced with increasing inertance, while the opposite happens at the secondary isolator. This observation confirms analytical results for the ideal 2-DOF linear system in Figure 1A reported in De Angelis et al.[23] demonstrating that the inertance leverages energy dissipated by the IVA

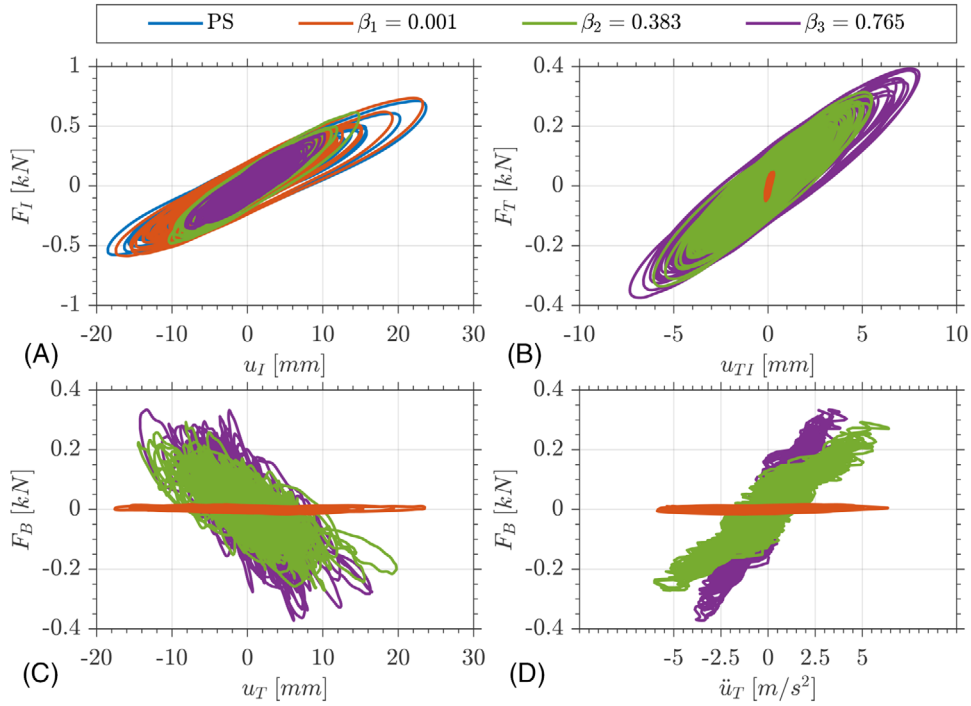

FIGURE 10 Force-deformation curves (A) $F_I - u_I$, (B) $F_T - u_{TI}$, (C) $F_B - u_T$, and (D) $F_B - \ddot{u}_T$ for BIS equipped with TMDI-configured IVAs with mass ratio $\mu = 0.080$ and various inertance ratios under random white noise excitation with A_2

and by the isolation layer in hybrid optimally designed TMDI-BIS systems. Accordingly, secondary isolator softens and exhibits increased displacement demands with increasing inertance while the opposite happens to the primary isolator. Last, inerter force displacement and force acceleration data plotted in Figure 10C and D confirm experimentally that the addition of flywheels to the inerter prototype used in the herein considered experiments increases the effective device inertance as quantified by the slope of the average backbone curves. The latter attains increasingly negative values in the inerter force displacement curves and increasingly positive values in the inerter force-acceleration curves.

4 | SEISMIC PERFORMANCE ASSESSMENT

In this section, pertinent experimental data are furnished to quantify the relative effectiveness of TMDI-configured IVAs with different inertial properties for motion control of the considered BIS under the shaking table excitations detailed in Section 2.3. For this purpose, the following 18 dimensionless seismic performance indices are adopted

$$\hat{p} = \frac{rms\,(p)}{rms\,(p_0)}, \bar{p} = \frac{\max\,(|p|)}{\max\,(|p_0|)}, p = u_I, u_{TI}, u_T, \ddot{u}_I^{(tot)}, \ddot{u}_T^{(tot)}, \ddot{u}_T, F_I, F_T, F_B, \tag{2}$$

where a hat over a symbol denotes root mean square (rms)-valued indices, a bar over a symbol denotes absolute peak-valued indices, and p_0 is u_{I0} for the displacements, $\ddot{u}_{I0}^{(\mathrm{tot})}$ for the acceleration, and F_{I0} for the forces with u_{I0}, $\ddot{u}_{I0}^{(\mathrm{tot})}$, and F_{I0} are the displacement, absolute acceleration, and base shear force of the uncontrolled BIS, respectively. In this respect, lower performance index values correspond to increased IVA effectiveness to reduce the seismic response quantity in the numerator of the index.

4.1 | Response to white noise excitation

Performance of TMDI-configured IVAs for white noise excitation is quantified in Figure 11 reporting nine different rms-valued performance indices defined in Equation (2) as a function of the inertance ratio and for the three secondary mass ratio values of the considered specimens. Indices in the first row of panels in Figure 11 assess performance with respect

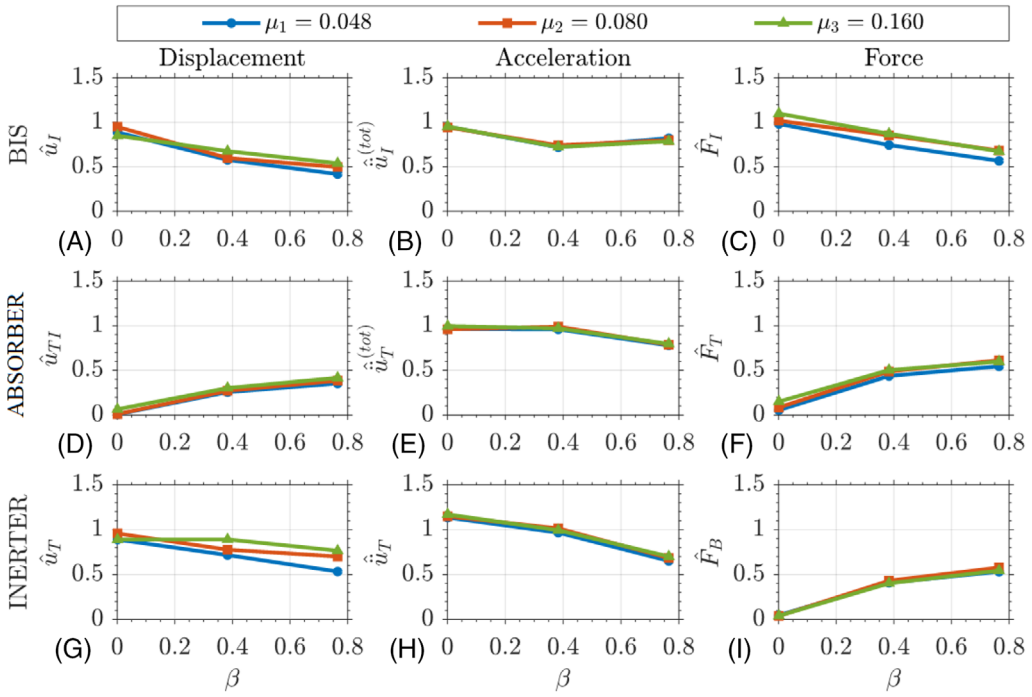

FIGURE 11 Performance indices versus inertance ratio β for BIS equipped with TMDI-configured IVAs with various values of mass ratio μ under white noise excitation with variance $\sigma^2_{\ddot{u}_G} = 0.916\ \mathrm{m}^2/\mathrm{s}^4$

to the BIS deflection, absolute acceleration, and base shear. The fact that all the indices are lower than 1 demonstrates the beneficial effect of nonoptimally designed TMDI to improve simultaneously all the above BIS response quantities. In particular, it is seen that both BIS rms deflection and base shear reduces significantly and monotonically with inertance reaching reductions up to 50 and 40%, respectively, for the highest inertance value examined. Further, the rms acceleration of BIS also improves compared to the uncontrolled structure, though not monotonically with the inertance, while absorbers with reduced mass ratio are more effective in reducing BIS deflections and base shear for fixed inertance. Importantly, all the above trends of the herein considered experimental data agree with trends from numerically derived data reported in the literature pertaining to white noise excited BISs equipped with TMDIs optimally designed using various optimization criteria.[20,23]

Turning the attention to rms response quantities of the attached mass and the inerter evaluated in the second and third row of panels in Figure 11, respectively, it is seen that, with the exception of the inerter displacement u_T, the secondary mass does not influence results. Both the inerter force and the control force exerted to the BIS increase with inertance at a reduced rate which explains the overall improved seismic performance of IVA-equipped BISs achieved with increasing inertance (first row of panels in Figure 11).

4.2 | Response to recorded ground motions

The TMDI-configured IVA potential for seismic protection of BISs is further assessed experimentally by examining all 18 performance indices in Equation (2) for the physical models with mass ratio $\mu = 0.08$ and inertance ratios $\beta_2 = 0.383$ and $\beta_3 = 0.765$ exposed to the six natural GMs in Table 2 unscaled and uniformly scaled by 2. Notably, results for the NF models ($\beta_1 = 0.001$) are not reported as they do not substantially defer from the uncontrolled BIS. Figures 12 and 13 report performance indices in terms of the rms and peak values with panels following the same 3-by-3 matrix layout as in Figure 11. Beneath each panel, response statistics (mean value and standard deviation) from the six unscaled GMs considered are reported separately for the two inertance values.

The average value from all GMs of the displacement and force-related indices in the first row of panels in Figures 12 and 13 follow the same trends with those observed for white noise excitation (first row of panels in Figure 11), as inertance increases from β_2 to β_3. This confirms the effectiveness of the absorber to reduce BIS deflection and base shear in terms of

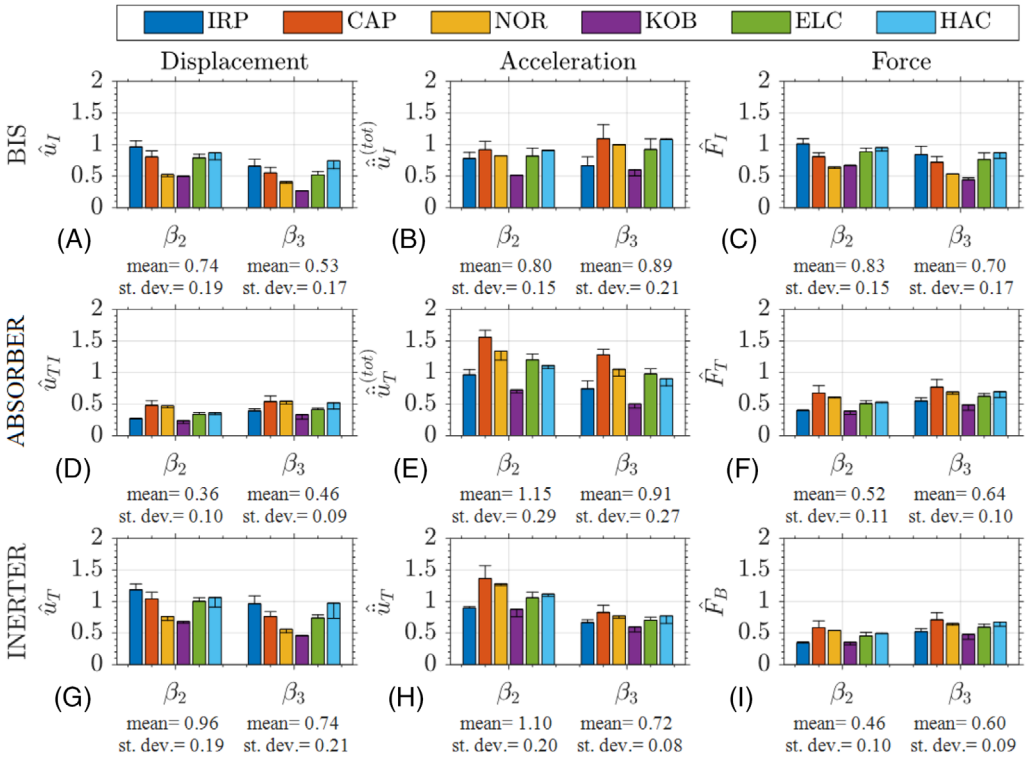

FIGURE 12 Performance indices in terms of rms value for BIS equipped with TMDI-configured IVAs with inertance ratios $\beta_2 = 0.383$ and $\beta_3 = 0.765$ and mass ratio $\mu = 0.08$ for the six GMs of Table 2. Boxes correspond to results for unscaled GMs and whiskers to GMs multiplied by 2. Statistics (mean and standard deviation) are for the unscaled GMs

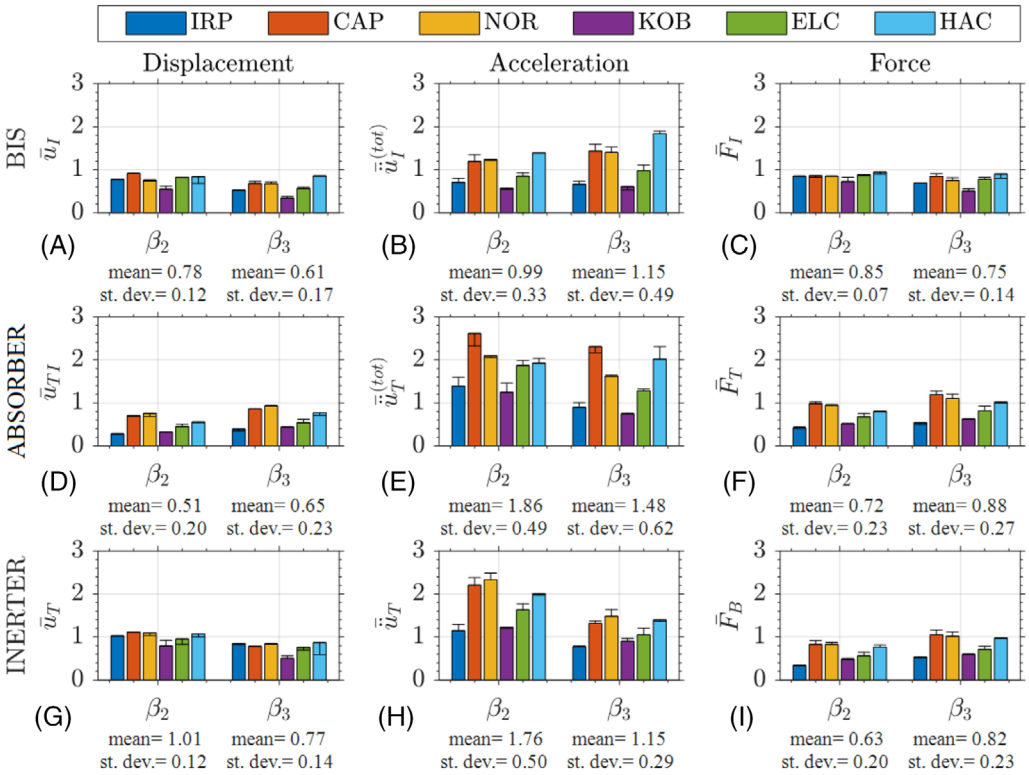

FIGURE 13 Performance indices in terms of absolute peak value for BIS equipped with TMDI-configured IVAs with inertance ratios $\beta_2 = 0.383$ and $\beta_3 = 0.765$ and mass ratio $\mu = 0.08$ for the six GMs of Table 2. Boxes correspond to results for unscaled GMs and whiskers to GMs multiplied by 2. Statistics (mean and standard deviation) are for the unscaled GMs

rms and peak values as inertance increases for different natural GMs. However, the level of these reductions varies widely among different GMs while reductions in peak values are always smaller from reductions in rms values. Specifically, the absorber is more effective on the average in reducing BIS deflection and base shear demands for the GMs recorded during the Northridge and Kobe seismic events, hereafter, NOR and KOB, respectively. The IVA with $\beta_3 = 0.765$ inertance ratio reduces rms and peak BIS deflection by 59 and 30%, respectively, for NOR scaled by 2, and by 73 and 60%, respectively, for KOB scaled by 2, while the corresponding percentage reductions for rms and peak BIS base shear are 48 and 18% for NOR scaled by 2, and 52 and 42% for KOB scaled by 2. On the antipode, IVA is least effective to reduce BIS deflection and base shear for the Irpinia record (IRP) in terms of rms values and for the Tokachi-Oki record (HAC) in terms of peak values. In detail, rms BIS deflection for the IRP scaled by 2 is 85% higher for the absorber with $\beta_3 = 0.765$ compared to the KOB GM scaled by 2, while no reduction to rms base shear is achieved compared to the uncontrolled BIS. Further, peak BIS deflection and base shear for the HAC scaled by 2 are 75 and 50% higher, respectively, for the absorber with $\beta_3 = 0.765$ compared to the KOB GM scaled by 2.

Even greater performance variability among different GMs is seen for peak BIS acceleration response in Figures 12B and 13B, respectively. In fact, the inclusion of the IVA affects negatively, for three out of the six GMs considered, the peak BIS acceleration (Figure 13B) as inertance increases. Similar detrimental effects of optimally designed TMD(I)s to BIS acceleration performance have been reported in the literature,[16,17,22,23] which relate to the (time-evolving) frequency content of GMs as reported by Taniguchi et al.[16] and De Angelis et al.[23] and discussed to more detail later in this section. In this regard, it is noted in passing that improved acceleration performance can be readily achieved in applications where this deemed important by optimally designing TMDI for minimizing structural acceleration.[20,52,53]

Commenting on the effect of GM amplitude on the performance indices related to the BIS response, it is seen that, in general, it has small influence to peak BIS deflection and base shear performance, while it mostly influences the rms BIS deflection and BIS acceleration indices, but this influence is GM dependent. For instance, rms BIS deflection performance index (Figure 12A) remains the same for NOR and KOB, reduces 17% for HAC and increases for the other three GMs upon scaling-up GMs by a factor of two. Still, the average influence of GM intensity is not significant and the previously discussed average trends in the performance indices remain.

Focusing next on performance indices related to secondary mass and inerter responses in the second and third rows of panels in Figures 12 and 13, it is observed that average trends across all the GMs coincide with those for white noise excitation: inerter force increases with inertance as well as relative displacement of secondary mass to BIS and, consequently, control force exerted to the BIS. These trends explain, intuitively, the improved BIS motion mitigation of absorbers with increasing inertance. On the antipode, mean values of inerter displacement and acceleration and of secondary mass acceleration reduce with inertance. In every case, large record-to-record variability is noted to the secondary mass and inerter response indices consistent with the variability observed in the indices related to the BIS performance indices. Additionally, a major increase is noted between the rms and the peak performance index values of the secondary mass and inerter accelerations. This increase is attributed to the shocks/pounding due to the play of the inerter prototype gears resulting in large instantaneous relative acceleration differences between the device terminals.

To shed light into the record-to-record variability of the performance indices in Figures 12 and 13, selective non-normalized experimental response time-histories are furnished in Figure 14 for the physical model with $\beta_2 = 0.383$ and $\mu_2 = 0.080$ subjected to NOR, KOB, IRP, and HAC GMs. On the same figure, the time-traces of the four GMs are included together with contour plots of GM energy distribution on the time-period plane with brighter colors indicating higher energy. The latter plots are obtained from standard continuous wavelet transform analysis applied to GM signals using Morlet wavelets as detailed in Torrence and Compo[54] and are considered to support dynamic response results interpretation.[23,55] The NOR energy distribution plot, shows significant GM energy early in time (at the beginning of the record) in the form of two relatively high-frequency "pulses" (with average period of about around 1/16 s = 0.0625 s) at 1.25 s and at 1.6 s time instants. Consequently, the absorber is not as effective to reduce peak BIS response, especially acceleration, for the NOR excitation due to the first pulse at the beginning of the record as there is not sufficient time to be activated. However, it is quite effective for reducing BIS response throughout time (ie, in the rms sense) as the absorber is mobilized by the first pulse: the fact that the second pulse is stronger in energy than the first pulse contributes to a relatively smooth energy build-up that reflects on the excellent rms BIS displacement reduction.

Based on the above reasoning, it is further possible to explain the overall excellent peak and rms BIS response reduction achieved by the IVA for the KOB GM. The energy of the latter GM is evenly distributed in time with dominant "patches" of energy at 0.75, 1.4, and at 2 s (most high-frequency patch at 1/32 s = 0.0313 s) having progressively higher

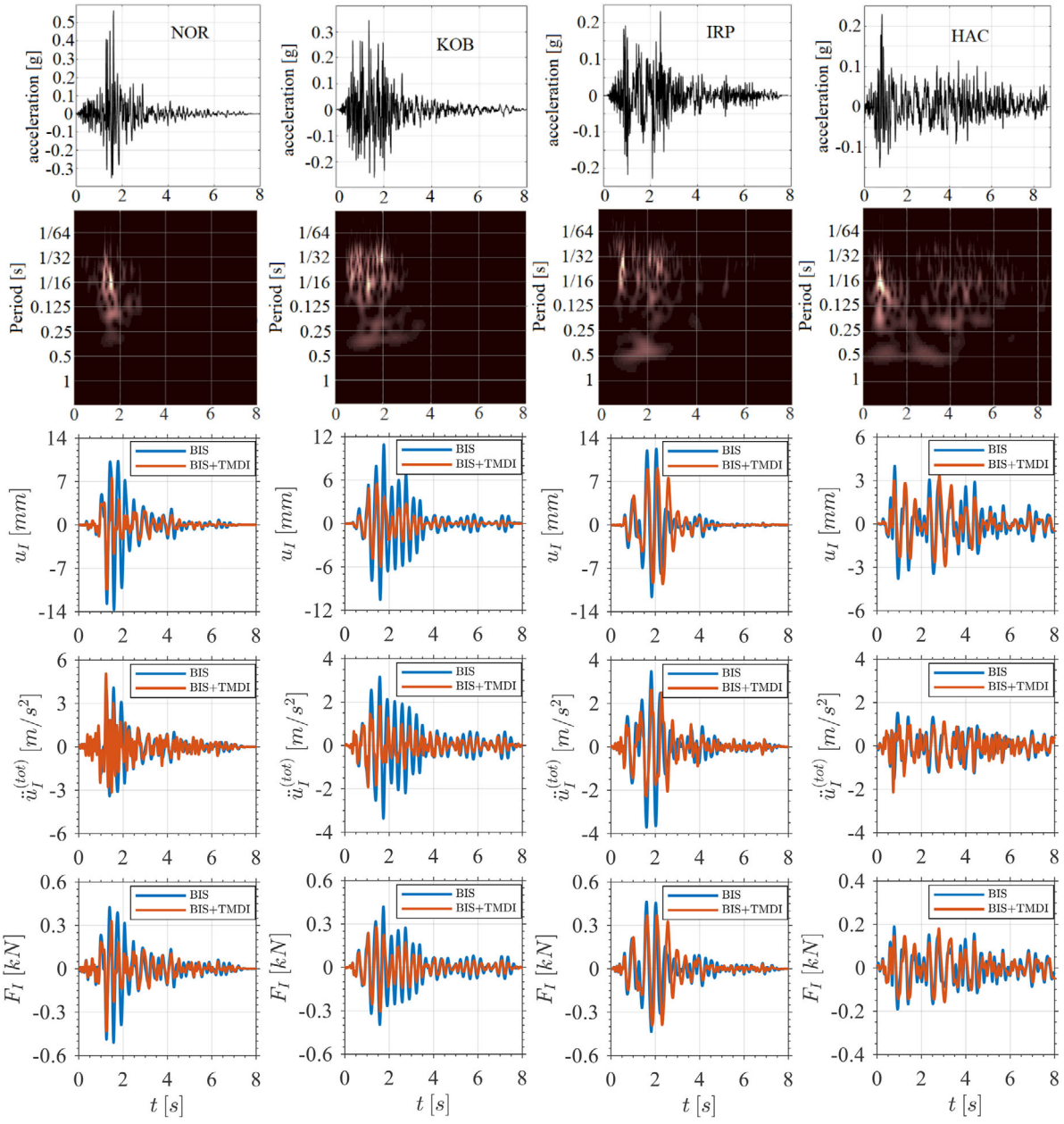

FIGURE 14 Time histories in terms of displacement u_I, acceleration $\ddot{u}_I^{(\text{tot})}$, and force F_I for uncontrolled BIS and for BIS equipped with TMDI-configured IVA with mass ratio $\mu = 0.080$ and inertance ratio $\beta = 0.383$ subject to four different GMs of Table 2

amplitude. This smooth energy build-up provides for the time to the absorber to be activated and, eventually, mitigate even acceleration response which is more sensitive to high-frequency input content. On the contrary, worst rms performance is for IRP due to a significant low-frequency (centered at 0.42 s period) late energy arrival (centered at 2 s time instant) which resonates with the first effective natural period of the TMDI controlled physical model at 2.2 Hz, as inferred from the FRFs in Figure 9 for β_2 inertance, but not for the uncontrolled BIS. Still, similar performance in terms of peak BIS displacement is noted for both IRP and NOR as both records contain a similar early sudden high-frequency energy signature. Last, the absorber is least effective on average for both rms and peak response mitigation for the HAC record which combines an early high-amplitude high-frequency content arrival (similar to NOR and IRP) together with sustained in time significant low-energy content centered at the first resonant period of the IVA-equipped BIS specimen.

For completeness, force-deformation curves of the uncontrolled BIS as well as of the BIS with TMDI for $\beta_2 = 0.383$ and $\mu_2 = 0.080$ are plotted in Figure 15 for the same four unscaled GMs considered in Figure 14. It is seen that reduced energy

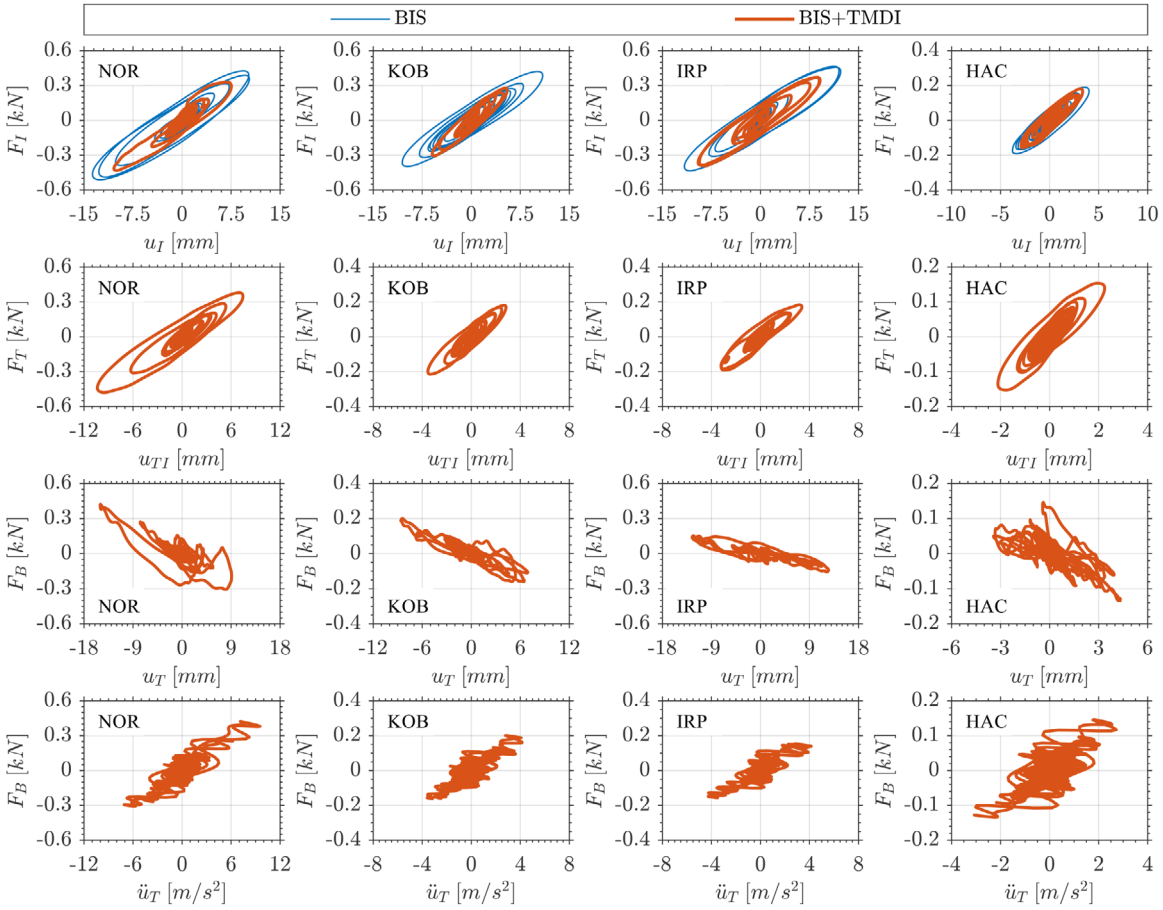

FIGURE 15 Force-deformation curves $F_I - u_I$, $F_T - u_{TI}$, $F_B - u_T$, and $F_B - \ddot{u}_T$ of BIS with and without TMDI with mass ratio $\mu = 0.080$ and inertance ratio $\beta = 0.383$ under various GMs of Table 2

dissipation occurs at the primary isolator for the controlled BIS compared to the uncontrolled one especially for the KOB GM which justifies previous observations on the high level of performance improvement achieved by the absorber for this GM. Further, significant deviation of the inerter device from the ideal inerter element behavior is observed under GM excitations especially when examining the inerter force-deformation curves (third row of panels in Figure 15). In this respect, the following section focuses on assessing the influence of the nonideal inerter behavior to the response of IVA-equipped BIS specimens with the aid of numerical models calibrated against experimental data.

5 | NONLINEAR NUMERICAL MODELLING AND INFLUENCE OF DISSIPATIVE INERTER TO BIS SEISMIC RESPONSE

Experimental inerter force-deformation curves in Figures 10 and 15 evidence that the inerter device prototype used in the shaking table tests dissipates energy under white noise and earthquake excitations, respectively, thus, deviating from the ideal inerter element.[46] Therefore, it is deemed essential to characterize the dissipative nature of the inerter prototype and to assess the influence of this characterization to the dynamic response of the BIS under earthquake excitation. To this aim, two different nonlinear 2-DOF parametric numerical models of the physical specimen with MF and secondary mass are considered whose effectiveness to capture the response of the specimens to harmonic excitations has been previously established in Pietrosanti et al.[41,42] The mechanical models are portrayed in Figure 16. Both the models use the same HDRB representation but differ in the level of sophistication by which the inerter device is modelled. One model uses the detailed nonlinear inerter modelling accounting for gearing backlash and friction effects in Figure 16B, while the other model uses the simplified equivalent linear inerter modelling in Figure 16C.

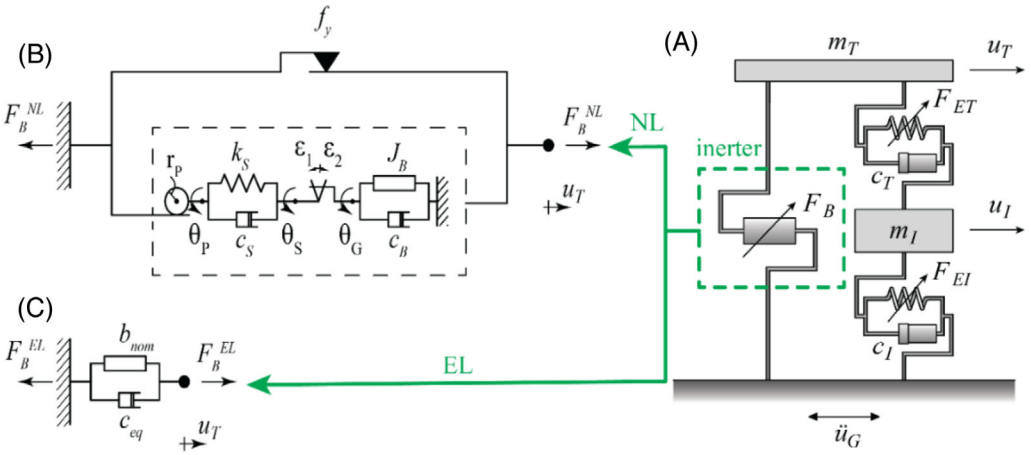

FIGURE 16 Mechanical models characterizing: (A) the physical system of Figure 1; (B) the inerter device using a nonlinear (NL) model; and (C) the inerter device using an equivalent linear (EL) model

Specifically, HDRBs are represented by a linear dashpot in parallel with a nonlinear element tracing a third-order polynomial function with deformation. Thus, the kinematic relationships of the HDRBs are written as[42]

$$\begin{aligned} F_{EI} &= k_{1I}u_I + k_{2I}u_I^2 sign\,(u_I) + k_{3I}u_I^3, F_{DI} = c_I\dot{u}_I \\ F_{ET} &= k_{1T}u_{TI} + k_{2T}u_{TI}^2 sign\,(u_{TI}) + k_{3T}u_{TI}^3, F_{DT} = c_T\,(\dot{u}_T - \dot{u}_I)\,, \end{aligned} \tag{3}$$

where F_{EI} and F_{DI} are the resisting forces of the nonlinear element and the dashpot, respectively, of the primary isolator, $F_{E\,T}$ and F_{DT} are the corresponding forces of the secondary isolator and $sign(x) = 1$ for $x > 0$ while $sign(x) = -1$ for $x < 0$. In the last expressions, k_{jI} and k_{jT} $(j = 1,2,3)$ are coefficients of the deformation-dependent element of the primary and secondary isolator, respectively, while c_I and c_T are the damping coefficients for the primary and secondary isolators, respectively.

Moreover, in the detailed inerter model of Figure 16B, r_P is the radius of the pinion transforming the translational, u_T, displacement (DOF) into rotational, θ_P, displacement (DOF), through $\theta_P = u_T/r_P$, while J_B is the flywheel moment of inertia (see also Figure 4). The model accounts for friction in the device rack-pinion mechanism using a Coulomb friction element with coefficient f_y, parasitic damping through a dashpot with coefficient c_B, and gearing backlash through a double-sided gap element with ε_1 and ε_2 clearances connected in series with a viscoelastic element with stiffness k_s and damping c_s.[42] The force-deformation relationship of the nonlinear inerter model is written as

$$F_B^{NL} = f_y sign(\dot{u}_T) + T_P/r_P, \tag{4}$$

where

$$\begin{cases} T_P = T_G \le 0\, for\, \theta_G - \theta_S = -\varepsilon_1 \\ T_P = T_G = 0\, for\, -\varepsilon_1 < \theta_G - \theta_S < \varepsilon_2\,, \\ T_P = T_G \ge 0\, for\, \theta_G - \theta_S = \varepsilon_2 \end{cases} \tag{5}$$

are relationships of the internal inerter device torques expressed by

$$T_P = k_S(\theta_S - \theta_P) + c_S(\dot{\theta}_S - \dot{\theta}_P)\, and\, T_G = J_B\ddot{\theta}_G + c_B\dot{\theta}_G, \tag{6}$$

in terms of the three internal device rotational DOFs, θ_P, θ_S, and θ_G, shown in Figure 16B.

The inerter force of the simplified inerter model in Figure 16C is taken as

$$F_B^{EL} = b_{nom}\ddot{u}_T + c_{eq}\dot{u}_T, \tag{7}$$

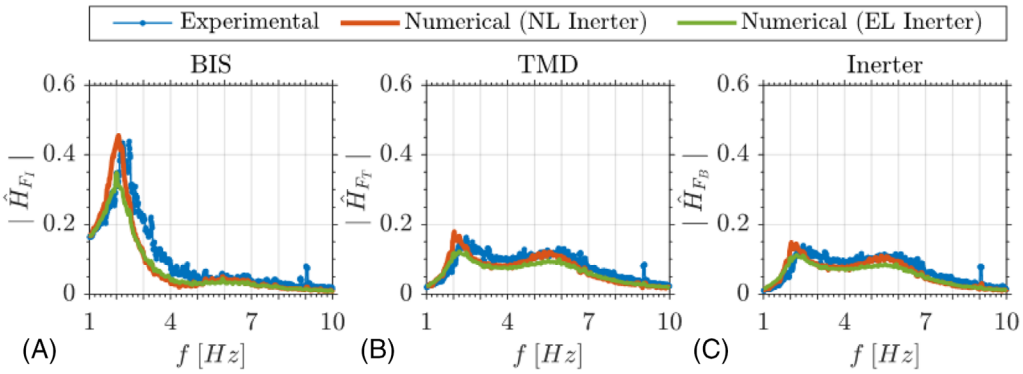

FIGURE 17 Comparison of experimental and numerical normalized FRFs of (A) Primary isolator force, (B) secondary isolator force, and (C) inerter force for BIS equipped with TMDI-configured IVA with mass ratio $\mu = 0.080$ and inertance ratio $\beta = 0.383$ for white excitation with amplitude A_2

where b_{nom} is the nominal inertance of the prototype as specified for each physical specimen in Section 2.1 and c_{eq} is an equivalent dashpot coefficient accounting for energy dissipation.

Overall, the equations of motion of the 2-DOF numerical models of Figure 16 are written as

$$\begin{aligned} m_I\ddot{u}_I + F_{EI} + F_{DI} &= -m_I\ddot{u}_G + F_{ET} + F_{DT}. \\ m_T\ddot{u}_T &= -m_T\ddot{u}_G - F_B - F_{ET} - F_{DT}. \end{aligned} \tag{8}$$

where $F_B = F_B^{NL}$ for the detailed inerter model and $F_B = F_B^{EL}$ for the simplified inerter model.

For the herein considered MF-MM specimen in Table 1, the mass properties of the numerical models in Figure 16 are $m_I = 125$ kg and $m_T = 10$ kg, while the properties of the NL inerter model are taken as $f_y = 7.3$ N, $r_P = 0.018$ m, $J_B = 1.55 \times 10^{-2}$ kgm^2, $k_S = 187.16$ Nm/rad, $c_S = 0.85$ Nms/rad,$\varepsilon_1 = 0.0084\,rad$, $\varepsilon_2 = 0.0056\,rad$ and $c_B = 0.03$ Nms/rad. These parameters have been determined by optimal fitting to experimental data obtained from inerter component-only harmonic shaking table testing. Further, the coefficients modelling the two HDRBs are determined as $k_{1I} = 3.94 \times 10^4$ N/m, $k_{2I} = -6.46 \times 10^5$ N/m^2, $k_{3I} = 4.52 \times 10^6$ N/m^3, $c_I = 538.13$ Ns/m, $k_{1T} = 5.55 \times 10^4$ N/m, $k_{2T} = -1.15 \times 10^6$ N/m^2, $k_{3T} = 8.48 \times 10^6$N/m^3 and $c_T = 409.15$ Ns/m by fitting the model with NL inerter in a standard least mean square sense to all nine FRFs defined in Equation (1) experimentally derived using sine-sweep excitations in Ref.[42]. The EL inerter model is defined by taking the nominal inertance $b_{nom} = 47.9$ kg (MF case) and the viscous coefficient $c_{eq} = 435.30$ Ns/m obtained by minimizing the sum of the squared differences between experimentally and numerically FRFs (see Refs.[41,42] for details).

Experimental and numerical force FRFs for white excitation with amplitude A_2 are compared in Figure 17 in which close point-wise matching is generally observed across frequencies with the exception of the resonant primary isolator frequency where the nonlinear inerter model overestimates peak shear force of the isolator, while the linear inerter model underestimates it. Still, the accuracy of the simplified inerter model to capture the experimental results does not fall much short of the accuracy of the much more complex nonlinear inerter model. Importantly, the latter finding holds true for the case of earthquake excitations. For illustration, Figure 18 provides comparison of time-history displacement and acceleration traces of the BIS as well as inerter force-deformation curves for the KOB and HAC GMs. It is seen that the model featuring the linear inerter element captures well experimental data with comparable accuracy to the nonlinear inerter model. This outcome, also confirmed for the rest of the speciments in Table 1 not presented here for the sake of brevity, signifies that nonlinearities in the inerter device do not affect much the response of BISs equipped with TMDI-configured IVAs. Therefore, the assumption of modelling the inerter device via simplified linear dissipative models may suffice in undertaking optimal TMDI design/tuning to minimise seismic response of BISs.

6 | CONCLUDING REMARKS

The response of BISs equipped with TMDI-configured IVAs under random white noise and earthquake base-excitations has been experimentally studied through shaking table testing to study the combined effects of nonlinear BIS and

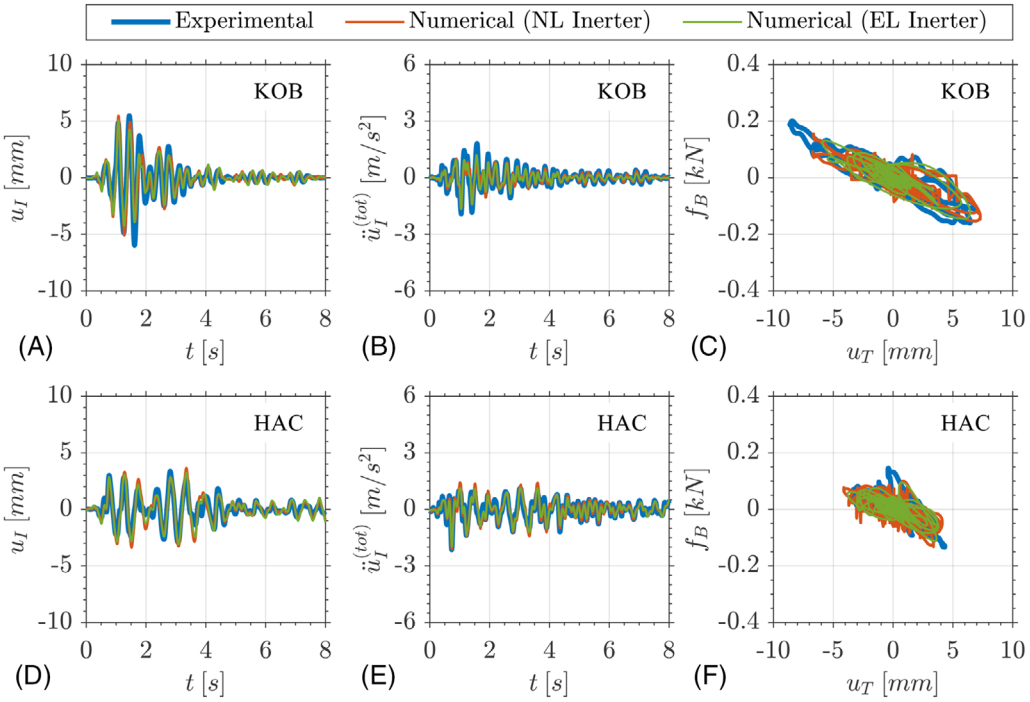

FIGURE 18 Comparison of experimental and numerical response of primary isolator displacement and acceleration time histories and inerter force-deformation curves for unscaled KOB and HAC GMs for BIS equipped with TMDI-configured IVA with mass ratio $\mu = 0.080$ and inertance ratio $\beta = 0.383$

absorber behaviour. To this aim, nonlinearly behaving HDRBs were used in the physical specimens to model the BIS and the absorber connection to the BIS while inertance was provided by a custom-built grounded rack-and-pinion flywheel inerter prototype. Comprehensive data were presented pertaining to a parametric experimental investigation involving nine specimens with different combination of IVA inertial properties (secondary mass and inertance) subject to white noise excitations for three different amplitudes and to six recorded GMs scaled at two different amplitudes. Stronger nonlinear elastic behavior of the softening kind with increasing excitation amplitude was verified for the HDRBs by noting changes to the resonant structural frequencies in FRFs obtained for white noise excitation as well as by inspecting experimental force-deformation curves for white noise and earthquake excitations. Further, the reported experimental force-relative acceleration and force-deformation curves for the inerter device exhibited significant deviation from the ideal inerter element attributed to friction and gear backlash effects. Yet, irrespective of the level of nonlinear behavior of the specimens, the experimental data verified the same motion control attributes of optimally designed TMDI found in previous theoretical studies assuming linear structural behavior and inerter element.[23] Specifically, the herein considered nonoptimal TMDI-configured IVAs become more effective in mitigating simultaneously BIS displacement and base shear response with increasing inertance and fixed secondary mass, but this is not necessarily the case for BIS acceleration. The inclusion of the IVA may be detrimental to the BIS peak and rms acceleration performance for GMs with early severe GM energy close to the BIS resonant frequency as captured by standard continuous wavelet transform spectrogram. On the other hand, the IVA improves significantly overall peak and rms BIS performance for GMs with smooth energy build-up irrespective of their dominant frequencies. Further, the positive IVA motion control effect of BIS response with increasing secondary mass saturates and, eventually, becomes insignificant with increasing inertance. In this respect, the significant practical advantage of inerter-based absorbers over conventional TMDs of overall improved seismic performance through increasing inertance rather than increasing secondary mass/weight leading to lightweight vibration absorbers extends to the case of nonlinear structures and inerter devices. Last, simulated data from two parametric numerical models of the specimens, one adopting a refined nonlinear mechanical model to represent the inerter device and the other a simplified linear dissipative model for the same, were found to be close to experimental seismic response data. This outcome suggests that the common assumption of modelling inerter devices by an ideal inerter element in parallel with a linear dashpot[36] suffices for optimal TMDI design and assessment used for seismic protection of BISs. Still, the above conclusions and recommendations have only been herein reached for TMDI with grounded inerter. In this respect, further experimental

research is warranted to address the case of TMDI-configured IVAs with nongrounded inerter[47] attached to possibly nonlinear behaving host structures under earthquake excitation. As a final remark, it is noted that the herein undertaken experimental campaign does not relate to any one particular base isolated structure designed for some site-specific seismic hazard. This consideration warrants further experimental research work which is expected to facilitate TMDI full-scale implementation in real-life structures.

ACKNOWLEDGMENTS

The financial support of Sapienza University of Rome under the Grant No. RP1181643697C751 (financial framework 2018), is gratefully acknowledged.

ORCID

Daniele Pietrosanti https://orcid.org/0000-0001-8927-3723
Maurizio De Angelis https://orcid.org/0000-0003-1896-3705

REFERENCES

1. Kunde MC, Jangid RS. Seismic behavior of isolated bridges: a-state-of-the-art review. *Electronic Journal of Structural Engineering*. 2003;3:140-170.
2. Pan P, Zamfirescu D, Nakashima M, Nakayasu N. Base-isolation design practice in Japan: introduction to the post-Kobe approach. *J Earthquake Eng*. 2005;9:147-171.
3. Warn GP, Ryan KL. A review of seismic isolation for buildings: historical development and research needs. *Buildings*. 2012;2:300-325.
4. Nagarajaiah S, Xiaohong S. Response of base-isolated USC hospital building in Northridge earthquake. *J. Struct. Eng. ASCE* 2000;126:1177-1186.
5. Wolff ED, Ipek C, Constantinou MC, Tapan M. Effect of viscous damping devices on the response of seismically isolated structures. *Earthquake Eng Struct Dyn*. 2015;44:185-198.
6. Whittaker AS, Kumar M, Kumar M. Seismic isolation of nuclear power plants. *Nuclear Engineering Technology*. 2014;46:569-580.
7. Kumar M, Whittaker AS, Constantinou MC. Extreme earthquake response of nuclear power plants isolated using sliding bearings. *Nucl Eng Des*. 2017;316:9-25.
8. Drozdov YN, Nadein VA, Puchkov VN. Seismic isolators for petroleum and gas platforms of the "Sakhalin-2" project. *Journal of Machinery Manufacture and Reliability*. 2010;39:591-604.
9. Paolacci F, Giannini R, De Angelis M. Seismic response mitigation of chemical plant components by passive control techniques. *Journal of Loss Prevention in the Process Industries*. 2013;26:924-935.
10. Reggio A, De Angelis M. Optimal design of an equipment isolation system with nonlinear hysteretic behaviour. *Earthquake Eng Struct Dyn*. 2014;42:1907-1930.
11. Reggio A, De Angelis M. Combined primary–secondary system approach to the design of an equipment isolation system with High-Damping Rubber Bearings. *J Sound Vib*. 2014;333:2386-2403.
12. Kitayama S, Constantinou MC. Probabilistic seismic performance assessment of seismically isolated buildings designed by the procedures of ASCE/SEI 7 and other enhanced criteria. *Eng Struct*. 2019;179:566-582.
13. Politopoulos I. A review of adverse effects of damping in seismic isolation. *Earthquake Eng Struct Dyn*. 2008;37:447-465.
14. Yang JN, Danielians A, Liu SC. A seismic hybrid control system for building structures. *J Eng Mech*. 1991;117:836-853.
15. Tsai HC. The effect of tuned-mass dampers on the seismic response of base-isolated structures. *Int J Solids Struct*. 1995;32:1195-1210.
16. Taniguchi T, Der Kiureghian A, Melkumyan M. Effect of tuned mass damper on displacement demand of base-isolated structures. *Eng Struct*. 2008;30:3478-3488.
17. Petti L, Giovanni G, De Luliis M, Palazzo B. Small scale experimental testing to verify the effectiveness of the base isolation and tuned mass dampers combined control strategy. *Smart Struct Syst*. 2010;6:57-72.
18. De Domenico D, Ricciardi G. Earthquake-resilient design of base isolated buildings with TMD at basement: application to a case study. *Soil Dyn Earthquake Eng*. 2018;113:503-521.
19. Hashimoto T, Fujita K, Tsuji M, Takewaki I. Innovative base-isolated building with large mass-ratio TMD at basement for greater earthquake resilience. *Fut Cit Environ*. 2015;1:1-19.
20. De Domenico D, Ricciardi G. An enhanced base isolation system equipped with optimal tuned mass damper inerter (TMDI). *Earthquake Eng Struct Dyn*. 2018;47:1169-1192.
21. De Domenico D, Ricciardi G. Improving the dynamic performance of base-isolated structures via tuned mass damper and inerter devices: a comparative study. *Struct Control Health Monit*. 2018c;25:e2234.
22. De Domenico D, Ricciardi G. Optimal design and seismic performance of tuned mass damper inerter (TMDI) for structures with nonlinear base isolation systems. *Earth Eng Struct Dyn*. 2018;47:2539-2560.

23. De Angelis M, Giaralis A, Petrini F, Pietrosanti D. Optimal tuning and assessment of inertial dampers with grounded inerter for vibration control of seismically excited base-isolated systems. *Eng Struct*. 2019;196:109250.
24. Smith MC. Synthesis of mechanical networks: the inerter. *IEEE Trans Automat Contr*. 2002;47:1648-1662.
25. Saitoh M. On the performance of gyro-mass devices for displacement mitigation in base isolation systems. *Structural Control and Health Monitoring*. 2012;19:246-259.
26. Marian L, Giaralis A. Optimal design of a novel tuned mass-damper-inerter (TMDI) passive vibration control configuration for stochastically support-excited structural systems. *Probabilist Eng Mech*. 2014;38:156-164.
27. Marian L, Giaralis A. The tuned mass-damper-inerter for harmonic vibrations suppression, attached mass reduction, and energy harvesting. *Smart Structures and Systems*. 2017;19:665-678.
28. Pietrosanti D, De Angelis M, Basili M. Optimal design and performance evaluation of systems with Tuned Mass Damper Inerter (TMDI). *Earthquake Engineering and Structural Dynamics* 2017;46:1367-1388.
29. Papageorgiou C, Houghton NE, Smith MC. Experimental testing and analysis of inerter devices. *Journal of Dynamic Systems, Measurement and Control*. 2008;131:011001.
30. Brzeski P, Lazarek M, Perlikowski P. Experimental study of the novel tuned mass damper with inerter which enables changes of inertance. *J Sound Vib*. 2017;404:47–57.
31. Watanabe Y, Ikago K, Inoue N, et al. Full-scale dynamic tests and analytical verification of a force-restricted tuned viscous mass damper. 15th World Conference on Earthquake Engineering, Lisbon, Portugal, 2012.
32. Nakamura Y, Fukukita A, Tamura K, et al. Seismic response control using electromagnetic inertial mass dampers. *Earthq Eng Struct Dynamics*. 2014;43:507-527.
33. Wang FC, Hong MF, Lin TC. Designing and testing a hydraulic inerter. *Proc Inst Mech Eng Part C J Mech Eng Sci*. 2011;225:66-72.
34. Nakaminami S, Kida H, Ikago K, Inoue N. Dynamic testing of a full-scale hydraulic inerter-damper for the seismic protection of civil structures. 7th International Conference on Advances in Experimental Structural Engineering, AESE 2017—Pavia, Italy 41-54. https://doi.org/10.7414/7aese.T1.55.
35. Swift SJ, Malcolm MC, Glover AR, Papageorgiou C, Gartner B, Neil HE. Design and modelling of a fluid inerter. *Int J Control*. 2013;86:2035-2051.
36. Liu X, Jiang JZ, Titurus B, Harrison A. Model identification methodology for fluid-based inerters. *Mech Syst Sig Process*. 2018;106:479-494.
37. Brzeski P, Perlikowski P. Effects of play and inerter nonlinearities on the performance of tuned mass damper. *Nonlinear Dyn*. 2017;88:1027-1041.
38. Lazar IF, Neild SA, Wagg DJ. Using an inerter-based device for structural vibration suppression. *Earthquake Eng Struct Dyn*. 2014;43:1129-1147.
39. De Domenico D, Deastra P, Ricciardi G, Sims ND, Wagg DJ. Novel fluid inerter based tuned mass dampers for optimised structural control of base-isolated buildings. *J Franklin Institute*. 2019;356:7626-7649.
40. Gonzales-Buelga A, Lazar IF, Jiang JZ, Neild SA, Inman DJ. Assessing the effect of nonlinearities on the performance of a tuned inerter damper. *Structural Control and Health Monitoring*. 2017;24:e1879.
41. Pietrosanti D, De Angelis M, Giaralis A. Shake table testing of a tuned mass damper inerter (TMDI)-equipped structure and nonlinear dynamic modeling under harmonic excitations. *In* Conference of the Italian Association of Theoretical and Applied Mechanics, Springer, Cham, 2019; 1512-1521.
42. Pietrosanti D, De Angelis M, Giaralis A. Experimental study and numerical modeling of nonlinear dynamic response of SDOF system equipped with tuned mass damper inerter (TMDI) tested on shaking table under harmonic excitation. *Int J Mech Sci*. 2020;184:105762.
43. Hoang N, Fujino Y, Warnitchai P. Optimal tuned mass damper for seismic applications and practical design formulas. *Eng Struct*. 2008;30(3):707-715.
44. De Angelis M, Giannini R, Paolacci F. Experimental investigation on the seismic response of a steel liquid storage tank equipped with floating roof by shaking table tests. *Earthq Eng Struct Dyn*. 2010;39:377-396.
45. Pietrosanti D, De Angelis M, Basili M. A generalized 2-DOF model for optimal design of MDOF structures controlled by Tuned Mass Damper Inerter (TMDI). *Int J Mech Sci*. 2020;185:105849.
46. Smith MC. The inerter: a retrospective. *Annu Rev Control Robot Auton Syst*. 2020;3:361-391.
47. Ruiz R, Taflanidis AA, Giaralis A, Lopez-Garcia D. Risk-informed optimization of the tuned mass-damper-inerter (TMDI) for the seismic protection of multi-storey building structures. *Eng Struct*. 2018;177:836-850.
48. Baker JW. Quantitative classification of near-fault ground motions using wavelet analysis. *Bull Seismic Soc Am*. 2007;97:1486-1501.
49. Ohtori Y, Christenson RE, Spencer BFJ, Dyke SJ. Benchmark structural control problems for seismically excited nonlinear buildings. *J Eng Mech*. 2004;130:366-385.
50. Luş H, Betti R, Longman RW. Obtaining refined first-order predictive models of linear structural systems. *Earthquake Eng Struct Dyn*. 2002;31:1413-1440.
51. Takewaki I, Murakami S, Yoshitomi S, Tsuji M. Fundamental mechanism of earthquake response reduction in building structures with inertial dampers. *Struct Control & Health Monitoring*. 2012;19:590-608.
52. Giaralis A, Taflanidis AA. Optimal tuned mass-damper-inerter (TMDI) design for seismically excited MDOF structures with model uncertainties based on reliability criteria. *Structural Control & Health Monitoring*. 2018;25:e2082.
53. Taflanidis AA, Giaralis A, Patsialis D. Multi-objective optimal design of inerter-based vibration absorbers for earthquake protection of multi-storey building structures. *J Franklin Institute*. 2019;356:7754-7784.

54. Torrence C, Compo GP. A practical guide to wavelet analysis. *Bull Amer Meteor*. 1998;79:61-78.
55. Spanos PD, Giaralis A, Politis NP, Roessett JM. Numerical treatment of seismic accelerograms and of inelastic seismic structural responses using harmonic wavelets. *Comput-Aided Civ Inf*. 2007;22:254-264.

How to cite this article: Pietrosanti D, De Angelis M, Giaralis A. Experimental seismic performance assessment and numerical modelling of nonlinear inerter vibration absorber (IVA)-equipped base isolated structures tested on shaking table. *Earthquake Engng Struct Dyn*. 2021;1–22. https://doi.org/10.1002/eqe.3469